

Pair annihilation radiation from relativistic jets in γ -ray blazars

M. Böttcher, R. Schlickeiser

Max-Planck-Institut für Radioastronomie, Postfach 20 24, 53 010 Bonn, Germany

Received ; accepted 06.07.1995

Abstract. The contribution of the pair annihilation process in relativistic electron-positron jets to the γ -ray emission of blazars is calculated. Under the same assumptions as for the calculation of the yield of the inverse Compton scattered photons by relativistic particles in the jet (Dermer and Schlickeiser 1993) we calculate the emerging pair annihilation radiation taking into account all spectral broadening effects due to the energy spectra of the annihilating particles and the bulk motion of the jet. It is shown that in spectral appearance the time-integrated pair annihilation spectrum appears almost like the well-known γ -ray spectrum from decaying π^0 -mesons at rest, since it yields a broad bumpy feature located between 50 and 100 MeV. We also demonstrate that for pair densities greater 10^9 cm^{-3} in the jet the annihilation radiation will dominate the inverse Compton radiation, and due to its bump-like spectrum indeed may explain reported spectral bumps at MeV energies. The refined treatment of the inverse Compton radiation including Klein-Nishina cross section corrections, the low-energy cutoff in the radiating relativistic particle distribution function and a realistic greybody accretion disk target photon spectrum leads to spectral breaks of the inverse Compton emission in the MeV energy range with a change in spectral index $\Delta\alpha$ larger than 0.5 as detected in PKS 0528+134 and 3C273.

Key words: Gamma rays – galaxies: nuclei – galaxies: active – black hole physics

1. Introduction

Until now 45 extragalactic γ -ray sources (status October 1994) have been clearly detected by the EGRET experiment aboard the Compton Observatory (Kanbach 1994, Thompson 1994). Several of them are also seen by the COMPTEL and OSSE instruments (Kurfess 1994). The broadband high energy spectra extend over four decades

Send offprint requests to: M. Böttcher

in energy and exhibit quite pronounced spectral forms and breaks. Apart from the Large Magellanic Cloud all extragalactic γ -ray sources are radio-loud, have a compact core and are known as highly variable sources. A large fraction of these sources exhibit apparent superluminal motion.

Because of its rapid variability, its high compactness, lack of radio-quiet sources in the sample and high presence of superluminal motion sources it is generally agreed (Blandford 1993, Dermer 1993, Dermer and Schlickeiser 1992, Dermer & Gehrels 1995) that the γ -ray emission originates in strongly beamed sources, in accord with the relativistic beaming hypothesis that has served well as the baseline model for the central engines of active galactic nuclei (Scheuer and Readhead 1979, Blandford and Königl 1979). Dermer and Schlickeiser (1993) - hereinafter referred to as DS - have demonstrated that at hard X-ray and γ -ray frequencies inverse Compton scattering of accretion disk photons by relativistic electrons and positrons in an outflowing plasma with relativistic bulk motion (bulk Lorentz factor $\Gamma \simeq 5 - 10$) dominates over other radiation mechanisms. This γ -ray production process successfully explains the key observational features as (i) the peak of the bolometric luminosity at γ -ray frequencies (ii) the γ -ray variability time scale \leq few days, (iii) the softening of the spectra between the hard X-ray and medium γ -ray regime, (iv) the high percentage of superluminal sources in the sample, (v) the generation of TeV emission for favourably aligned observers.

It has been suggested (Henri, Pelletier & Roland 1993) that pair annihilation in relativistic electron-positron jets could be of considerable importance to such jet models. The purpose of this study is thus to extend the DS-model by including the γ -ray production from pair annihilation radiation from relativistic jets. Under the same assumptions as for the calculation of the inverse Compton scattering from the jet we will determine the yield of annihilation radiation. Of special interest will be the modelling of spectral breaks with a change in spectral index $\Delta\alpha$ larger than 0.5 as detected in PKS 0528+134, $\Delta\alpha = 1.16(+0.23, -0.11)$ and 3C273, $\Delta\alpha = 0.66(+0.13, -0.15)$.

In the original DS approach spectral breaks up to $\Delta\alpha \leq 0.5$ were obtained by incomplete inverse Compton cooling of an injected power law during the time evolution of the γ -ray flare. Taking into account all spectral broadening effects due to the energy spectra of the annihilating particles and the bulk motion of the jet, we show here that the contribution from this radiation component peaks near a few MeV, and if it dominates the inverse Compton component it may provide an explanation for the reported spectral maxima in this energy range.

2. Jet model for the γ -ray emission

The jet model for the γ -ray emission in AGNs of DS is illustrated in Figure 1. Relativistic electrons and positrons, with isotropic energy distribution functions $n_{\pm}(\gamma; z)$ in the comoving frame at height z above the accretion disk, flow outward along the disk symmetry axis with bulk Lorentz factor Γ and bulk velocity $\beta_{\Gamma}c$ from an initial height z_i . Photons produced by the accretion disk pass through the jet and are Compton upscattered to γ -ray energies $km_e c^2$ (see DS for details). The relativistic electrons and positrons fill not the whole jet but only an (assumed) spherical blob of radius R_B . We follow the notation of DS: energies and angles without asterisks denote values in the comoving fluid frame, while these quantities with asterisks denote values in the stationary frame K of the accretion disk. We do not include cosmological effects here.

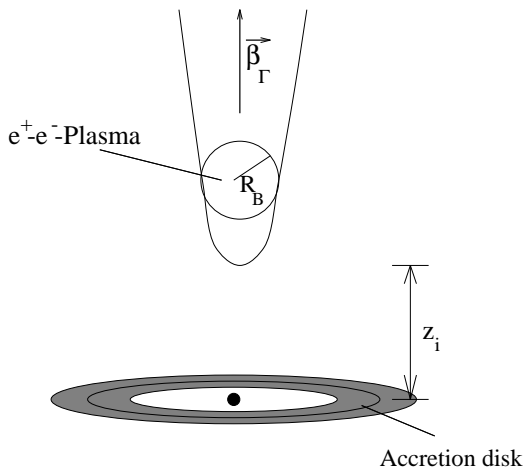


Fig. 1: Jet model for the γ -ray emission in AGNs

To avoid heavy attenuation of the produced GeV γ -rays by pair production interactions with the accretion disk photons Dermer and Schlickeiser (1994) have pointed out that the initial height of the blob has to be larger than $z_p = 10^{15}(L_{46}/\Theta_{50})^{1/2}$ cm where L_{46} denotes the accretion disk luminosity in units of 10^{46} erg/s and Θ_{50} the accretion disk temperature in units of 50 eV. Such a high location of the blob is also consistent with the presence of

many superluminal motion sources in the sample of γ -ray blazars. At these heights the pair annihilation radiation freely escapes from the system and does not initiate a pair cascade (Lightman and Zdziarski 1987, Zdziarski et al. 1990, Protheroe et al. 1992) with plenty production of 511 keV annihilation line radiation from the cascade-cooled cold electron-positron pairs that is not observed from these objects (Kurfess 1994). As in DS we start with initial relativistic power law energy spectra for the radiating particles

$$n_{\pm}(\gamma_{\pm}, z_i) = N_{\pm} \gamma_{\pm}^{-s} \quad 1 \ll \gamma_{1\pm} \leq \gamma_{\pm} \leq \gamma_{2\pm}, \quad (1)$$

and follow the time evolution of the energy spectra under the various energy loss processes. These spectra are used to calculate the yield of annihilation radiation at various heights. We start our analysis with the calculation of the annihilation radiation emissivity.

3. Pair annihilation radiation from the electron-positron blob

The general calculation of the yield of pair annihilation radiation from relativistic plasmas has been treated by Svensson (1982). In the case of an ultrarelativistic pair plasma, characterised by Eq. (1), this treatment can be considerably simplified by using the differential pair annihilation cross section

$$\left(\frac{d\sigma}{d\Omega_{cm}}\right)_{rel} = \frac{r_e^2}{4\gamma_{cm}^2} \left\{ -1 + \left(\frac{1}{1 - \beta_{cm}x} + \frac{1}{1 + \beta_{cm}x} \right) \right\} \quad (2)$$

which is valid for $\gamma_{cm} \gg 1$. The subscript cm denotes quantities measured in the center-of-momentum frame and $x = \frac{\vec{k}_{cm} \cdot \vec{\beta}_{cm}}{k_{cm} \beta_{cm}}$. Then, following the calculation leading to Svensson's formulae (55) – (57) yields

$$\left(\frac{d\sigma}{dk}\right)_{rel} = \pi r_e^2 \left(-\frac{1}{\gamma_{cm}^2 \sqrt{(\gamma_+ + \gamma_-)^2 - 4\gamma_{cm}^2}} + \frac{2}{\gamma_{cm} \sqrt{\gamma_{cm}^{*2} + c_+ \gamma_{cm}^2}} + \frac{2}{\gamma_{cm} \sqrt{\gamma_{cm}^{*2} + c_- \gamma_{cm}^2}} \right) \quad (3)$$

— where

$$c_{\pm} = (k - \gamma_{\mp})^2 - 1, \quad (4)$$

$$\gamma_{cm}^{*2} = k(\gamma_+ + \gamma_- - k), \quad (5)$$

k is the photon energy normalized to the electron rest energy, the subscript \pm denotes quantities referring to the motion of the positron/electron as measured in the labor frame (the rest frame of the plasma blob) and γ_{cm}^* is the maximum center-of-momentum γ -factor in the case of

which a photon of energy k can be produced, which is the notation used by Svensson (1982) — and

$$\left(v \frac{d\sigma}{dk} \right)_{rel} (k, \gamma_+, \gamma_-) = \frac{c \pi r_e^2}{\gamma_+^2 \gamma_-^2} \cdot \left(\sqrt{(\gamma_+ + \gamma_-)^2 - 4\gamma_{cm}^2} + H_+ + H_- \right) \Big|_{\gamma_{cm}^L}^{\gamma_{cm}^U} \quad (6)$$

where the bar denotes the averaging over collision angles between $\vec{\beta}_+$ and $\vec{\beta}_-$ and

$$H_{\pm} = \frac{\gamma_{cm}}{c_{\pm}} \sqrt{\gamma_{cm}^{*2} + c_{\pm} \gamma_{cm}^2} + \frac{\gamma_{cm}^{*2}}{|c_{\pm}|^{3/2}} \cdot \begin{cases} \arcsin \left(\frac{\sqrt{-c_{\pm}} \gamma_{cm}}{\gamma_{cm}^*} \right) & \text{for } c_{\pm} < 0 \\ -\operatorname{arsinh} \left(\frac{\sqrt{c_{\pm}} \gamma_{cm}}{\gamma_{cm}^*} \right) & \text{for } c_{\pm} > 0 \end{cases}, \quad (7)$$

$$H_{\pm} = \frac{2}{3} \frac{\gamma_{cm}^3}{\gamma_{cm}^*} \quad \text{for } c_{\pm} = 0 \quad (8)$$

Also the integration limits $\gamma_{cm}^U, \gamma_{cm}^L$ which are determined by kinematical restrictions may be simplified. As given by Svensson (1982) these integration limits are found to be

$$\gamma_{cm}^L = \gamma_{cm}^{min} = \sqrt{\frac{1}{2} (1 + \gamma_+ \gamma_- [1 - \beta_+ \beta_-])} \quad (9a)$$

$$\gamma_{cm}^U = \min \{ \gamma_{cm}^{max}, \gamma_{cm}^* \} \quad (9b)$$

where

$$\gamma_{cm}^{max} = \sqrt{\frac{1}{2} (1 + \gamma_+ \gamma_- [1 + \beta_+ \beta_-])} \quad (10)$$

is the center-of-momentum γ -factor in the case of head-on collision which, for $\beta_+, \beta_- \approx 1$, simplifies to $\gamma_{cm}^{max} \approx \sqrt{\gamma_+ \gamma_-}$. γ_{cm}^{min} is the minimum center-of-momentum Lorentz factor in the case of an overtaking collision. Writing $\gamma_{cm}^{*2} = \gamma_+ \gamma_- - (k - \gamma_-)(k - \gamma_+)$, we immediately see that

$$\gamma_{cm}^U = \begin{cases} \gamma_{cm}^{max} & \text{for } (k > \gamma_+ \wedge k < \gamma_-) \text{ or } (k < \gamma_+ \wedge k > \gamma_-) \\ \gamma_{cm}^* & \text{for } (k < \gamma_+ \wedge k < \gamma_-) \text{ or } (k > \gamma_+ \wedge k > \gamma_-) \end{cases} \quad (11)$$

Furthermore, we have to satisfy the condition

$$k < k_U \\ = \frac{1}{2} (\gamma_+ [1 + \beta_+] + \gamma_- [1 + \beta_-]) \quad (12)$$

where k_U is the maximum photon energy available by the annihilation of an e^+e^- -pair characterized by γ_+, γ_- (Svensson 1982). In the ultrarelativistic case, equation

(12) simply becomes $k < \gamma_+ + \gamma_-$ which is equivalent to the condition $\gamma_{cm}^{*2} > 0$.

Unfortunately, equation (6) is still not analytically integrable, but for $\gamma_{1+}, \gamma_{1-} \gtrsim 5$, it may be very well used for numerical calculations of the integral

$$\left\langle v \frac{d\sigma}{dk} \right\rangle (k) \\ = \int_{\gamma_{1+}}^{\gamma_{2+}} d\gamma_+ \int_{\gamma_{1-}}^{\gamma_{2-}} d\gamma_- f_+(\gamma_+) f_-(\gamma_-) \overline{v \frac{d\sigma}{dk}} (k, \gamma_+, \gamma_-) \quad (13)$$

(Svensson 1982) where the brackets denote the averaging over the distribution functions of electrons and positrons.

For further simplifications, we use the fact that in Eq. (6) only the upper limit γ_{cm}^U is important and also the first term is negligible as compared to the values of $H_{\pm}(k, \gamma_{cm}^U, \gamma_{cm}^*)$. As mentioned by Svensson, for highly relativistic pair plasmas, the angle averaged emissivity is sharply peaked at $\gamma_+ = k$ and $\gamma_- = k$ where the photon takes over the energy and momentum of the incoming positron or electron, respectively. We use this fact to approximate $v \frac{d\sigma}{dk}$ by constructing a function that satisfies the condition of these peak values and exhibits the same asymptotical behavior as found for $v \frac{d\sigma}{dk}$.

The well-known δ -function approximation does not work well in the case of an energy distribution as given by eq. (1), particularly, it does not describe the lower energy tail of the annihilation spectrum ($k < \min \{ \gamma_{1+}, \gamma_{1-} \}$) at all. The approximation scheme we derive here is much simpler than that given by Coppi and Blandford (1990) who still need numerical integrations to determine the dispersion of $v \frac{d\sigma}{dk}$ about k but whose results are — in contrast to ours — also valid for mildly relativistic pair plasmas.

The peak values of H_{\pm} as given by eq. (6) are easily found by setting $c_{\pm} = -1$ and $\gamma_{cm}^U = \gamma_{cm}^* = \sqrt{\gamma_+ \gamma_-}$:

$$H_{\pm}(k, \gamma_{cm}^U) \Big|_{c_{\pm} = -1} = \frac{\pi}{2} (\gamma_{cm}^U)^2. \quad (14)$$

Considering the asymptotic behavior of $v \frac{d\sigma}{dk}$, we see that for $|k - \gamma_{\pm}| \gg 1$ the photon is not emitted in the direction of the incoming electron/positron, and so x does not approach 1 where the differential cross section (2) peaks. For this reason, we may set $\beta_{cm} = 1$ in eq. (2) and in the following steps of calculation, which yields

$$\overline{v \frac{d\sigma}{dk}} (k, \gamma_+, \gamma_-) \Big|_{c_{\pm} \gg 1} = \frac{(\gamma_{cm}^u)^2}{|k - \gamma_{\mp}|}. \quad (15)$$

A quite simple function combining the characteristics described by eqs. (14) and (15) and therefore approximating $v \frac{d\sigma}{dk}$ is

$$\left(v \frac{d\sigma}{dk} \right)_{rel} (k, \gamma_+, \gamma_-) \approx \frac{c\pi r_e^2}{\gamma_+^2 \gamma_-^2} \cdot \left[\frac{(\gamma_{cm}^U)^2}{|k - \gamma_+| + \frac{2}{\pi}} + \frac{(\gamma_{cm}^U)^2}{|k - \gamma_-| + \frac{2}{\pi}} \right]. \quad (16)$$

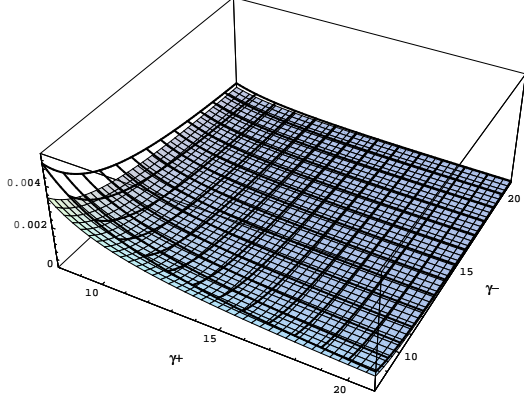


Fig. 2: Asymptotic approximation (16) (transparent area) in comparison to the relativistic value of $v \frac{d\sigma}{dk}$ calculated by eq. (6) (gray area) for $k = 4$

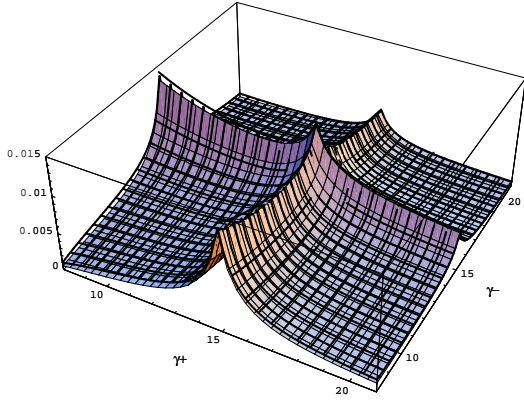


Fig. 3: Same as Fig. 2, but for $k = 15$

We call it the asymptotic approximation. Figures 2 – 4 show that Eq. (16) is a very useful approximation to the angle averaged emissivity from highly relativistic pair plasmas for $k \gtrsim \min\{\gamma_{1+}, \gamma_{1-}\}$, but which is — in contrast to the δ -function approximation — still sensible for $k < \min\{\gamma_{1+}, \gamma_{1-}\}$.

By means of a series expansion of the asymptotic approximation, the integrations in eq. (13) are elementary for power-law distributions (1) and are also analytically executable for other physically relevant ultrarelativistic

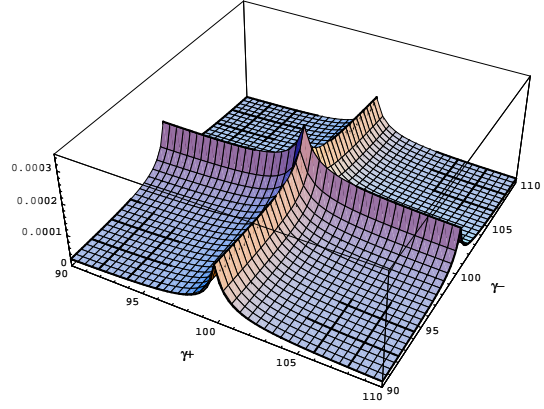


Fig. 4: Same as Figs. 2 and 3 for $k = 100$

distribution functions. Due to different determinations of $v \frac{d\sigma}{dk}$ in the four integration areas defined by Eq. (11), the results look somewhat involved, but they are — after some manipulations — numerically quite simply evaluable.

Expanding (16) in a series and performing the integral (13) — where we neglect the integration area given by the edge points $(\gamma_{\pm}, \gamma_{\mp}) = (k, k - \gamma_{1\pm}), (k, \gamma_{1\pm}), (\gamma_{1\pm}, k - \gamma_{1\mp}), (\gamma_{1\mp}, k - \gamma_{1\pm}), (\gamma_{1+}, k)$ for integration over $\frac{1}{\frac{2}{\pi} + |k - \gamma_{\pm}|}$ — yields

$$\begin{aligned} \left\langle v \frac{d\sigma}{dk} \right\rangle_{rel} (k) = & \Theta(k - \gamma_{1-}) \Theta(k - \gamma_{1+}) \left(\frac{\gamma_{1-}^{-s} - (\min\{k, \gamma_{2-}\})^{-s}}{s} \right. \\ & \cdot [S_1(\min\{k, \gamma_{2+}\}, s + 1) - S_1(\max\{\gamma_{1+}, k - \gamma_{1-}\}, s + 1)] \\ & + \frac{\gamma_{1-}^{-(s+1)} - (\min\{k, \gamma_{2-}\})^{-(s+1)}}{s + 1} \\ & \cdot [S_1(\min\{k, \gamma_{2+}\}, s) - S_1(\max\{\gamma_{1+}, k - \gamma_{1-}\}, s) \\ & \quad - k \{S_1(\min\{k, \gamma_{2+}\}, s + 1) \\ & \quad \left. - S_1(\max\{\gamma_{1+}, k - \gamma_{1-}\}, s + 1)\}] \right) \quad (17a) \end{aligned}$$

$$\begin{aligned} & + \Theta(\gamma_{2-} - k) \Theta(k - \gamma_{1+}) \frac{(\max\{k, \gamma_{1-}\})^{-s} - \gamma_{2-}^{-s}}{k s} \\ & \cdot (S_1(\min\{k, \gamma_{2+}\}, s) - S_1(\gamma_{1+}, s)) \quad (17b) \end{aligned}$$

$$\begin{aligned} & + \Theta(k - \gamma_{1-}) \Theta(\gamma_{2+} - k) \frac{(\min\{k, \gamma_{2-}\})^{-s} - \gamma_{1-}^{-s}}{s} \\ & \cdot (S_2(\gamma_{2+}, s + 1) - S_2(\max\{k, \gamma_{1+}\}, s + 1)) \quad (17c) \end{aligned}$$

$$\begin{aligned} & + \Theta(\gamma_{2-} - k) \Theta(\gamma_{2+} - k) \left(\frac{\gamma_{2-}^{-s} - (\max\{k, \gamma_{1-}\})^{-s}}{s} \right. \\ & \quad \left. \cdot k (S_2(\gamma_{2+}, s + 2) - S_2(\max\{k, \gamma_{1+}\}, s + 2)) \right) \end{aligned}$$

$$\begin{aligned}
& + \frac{\gamma_{2-}^{-(s+1)} - (\max\{k, \gamma_{1-}\})^{-(s+1)}}{s+1} k \cdot \\
& \cdot \left(S_2(\gamma_{2+}, s+1) - S_2(\max\{k, \gamma_{1+}\}, s+1) \right. \\
& \left. - k [S_2(\gamma_{2+}, s+2) - S_2(\max\{k, \gamma_{1+}\}, s+2)] \right) \quad (17d) \\
& + [+ \leftrightarrow -]
\end{aligned}$$

where $[+ \leftrightarrow -]$ denotes the preceding terms (17 a) – (17 d) under transposition of the subscripts $+ \leftrightarrow -$, Θ is the Heaviside function and

$$S_1(\gamma, s) = \gamma^{-s} \sum_{\substack{n=0 \\ n \neq s}}^{\infty} \frac{1}{n-s} \left(\frac{\gamma}{\kappa_+} \right)^n + \delta_{s,N} k^{-s} \ln(\gamma) \quad (18a)$$

$$S_2(\gamma, s) = \gamma^{-s} \sum_{n=0}^{\infty} \frac{1}{n+s} \left(\frac{\kappa_-}{\gamma} \right)^n, \quad (18b)$$

with the symbol $\delta_{s,N}$ defined by

$$\delta_{s,N} = \begin{cases} 1 & \text{for } s \in \mathbb{N} \\ 0 & \text{for } s \notin \mathbb{N} \end{cases} \quad (19)$$

and $\kappa_{\pm} = k \pm \frac{2}{\pi}$. Of course, we must not replace κ_{\pm} by k in eqs. (18), because the series S_1 and S_2 would diverge then. The series S_1 is easily evaluable by summing several ($> s$) terms and replacing the remaining part of the sum by the integral whose upper Riemann sum it is, while S_2 may be evaluated by subtracting a geometrical series whose value is known, with the remaining series converging very quickly.

Doing so, we see that Eq. (17) provides a very accurate approximation to the pair annihilation spectrum. In Fig. 5, this approximation is compared to the results of numerical integrations over the exact solution for $v \frac{d\sigma}{dk}$ given by Svensson (1982). Especially the peak structure and the high energy tail of the spectrum are very well described by the asymptotic approximation, while also the low energy tail is sensibly approximated, considering that this part of the spectrum — as compared to spectra produced by other radiation mechanisms resulting mainly in power laws — will not be very important. Note that the different absolute values of the peak emissivity for different spectral indices is caused by the fact that for simplicity we used not normalized distribution functions with $N_{\pm} = 1$.

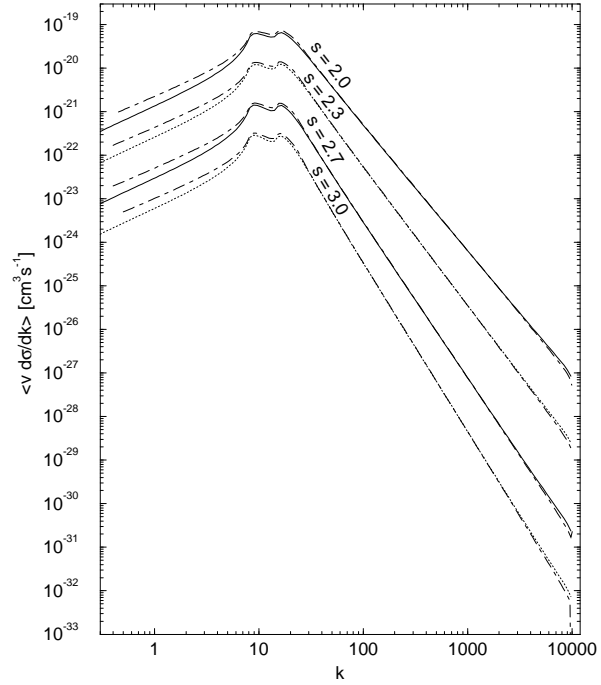


Fig. 5: Pair annihilation spectra calculated by the asymptotic approximation (17) (dashed) compared to numerical integrations (solid and dotted, respectively); parameters: $\gamma_{1+} = 8$, $\gamma_{1-} = 15$, $\gamma_{2-} = \gamma_{2+} = 10^4$

4. Particle spectra evolution

We now consider the evolution of an ensemble of particles that is injected at height z_i with a power law distribution in energy given by Eq. (1). We first treat the effects of inverse-Compton, synchrotron bremsstrahlung and pair annihilation losses separately in order to achieve an estimate for typical timescales for the deviation from an initial power law distribution caused by each one of these processes.

The typical peak structure of annihilation radiation is mainly caused by the lower energy end of particle distributions. Therefore we show that energy loss mechanisms most effectively cooling high energy particles ($\gamma_{\pm} \gg \gamma_{1\pm}$) may not seriously influence the shape of the annihilation spectrum during the evolution of the particle spectrum. So, the typical timescale for low energy particle spectra evolution may be significantly longer than the timescale for energy losses by a single particle.

Note that this does not represent a realistic calculation of the particle spectra evolution — this will be treated in future work —, but gives only a rough estimate of the typical timescale on which the assumption of a power law distribution of particle energies is justified.

4.1. Inverse Compton losses

The effect of inverse Compton losses on particle energy spectra in the jet has been treated in DS. There, a typical particle energy γ_∞ is defined by

$$\gamma_\infty = \frac{\tilde{z}_i}{2488 \ell_0} \beta_\Gamma \Gamma^3 (1 + \beta_\Gamma)^2 \quad (20)$$

where the tilde denotes the normalization to gravitational radii — $\tilde{z} = \frac{z}{R_g}$, $R_g = \frac{GM}{c^2}$ — and $\ell_0 = \frac{L_0}{L_{edd}}$. It is shown that particles with energy greater than γ_∞ are suffering heavy losses while the spectral shape of particles with energy $\gamma_\pm < \gamma_\infty$ remains nearly unaffected by inverse Compton losses. This spectral evolution which, of course, does not depend on the particles' charge is shown in Fig. 6.

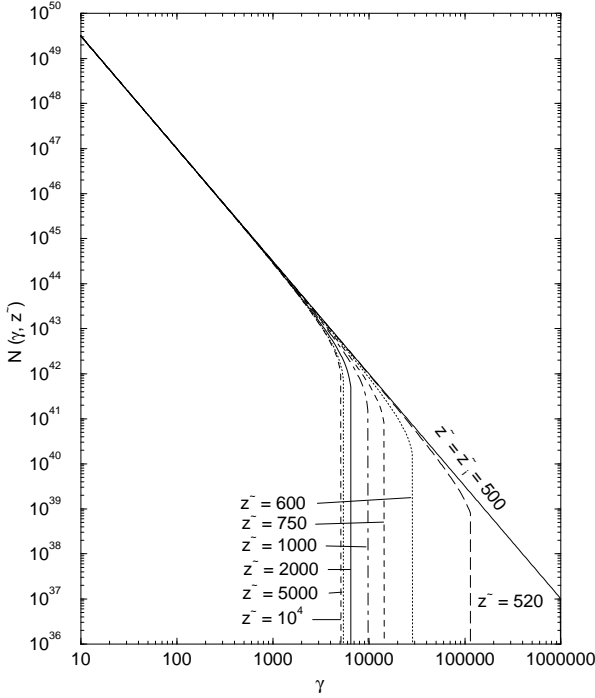


Fig. 6: Evolution of a power law particle spectrum, affected by inverse-Compton losses. Parameters: $\tilde{z}_i = 500$, $\gamma_{1\pm i} = 10$, $\gamma_{2\pm i} = 10^6$, $s = 2.5$, $M_8 = 1$, $\ell_0 = 0.1$.

From Eq. (20) and Fig. 6, we conclude that the shape of the low energy particle spectrum will not be altered substantially by inverse Compton losses, and therefore the pair annihilation peak structure will not strongly depend on particle spectra evolution caused by the inverse Compton process.

4.2. Synchrotron losses

In order to investigate the effect of synchrotron losses we use the single particle energy loss rate due to the synchrotron process

$$-mc^2 \dot{\gamma}_\pm = \frac{4}{3} \sigma_T \frac{B^2}{8\pi} c \beta_\pm^2 \gamma_\pm^2 \quad (21)$$

— where B is the magnetic field strength which we assume to be approximately constant — combined with the blob's equation of motion

$$\tilde{z}(t^*) = \tilde{z}_i + \frac{c\beta_\Gamma t^*}{R_g} \quad (22)$$

and the time-dilation $\delta t^* = \Gamma \delta t$. This yields

$$\left(\frac{d\gamma_\pm}{d\tilde{z}} \right)_{s_y} = -\frac{4}{3} \frac{\sigma_T B^2}{8\pi m c^2} \frac{R_g}{\Gamma \beta_\Gamma} \gamma_\pm^2 =: -K \gamma_\pm^2. \quad (23)$$

where

$$K = 5 \cdot 10^{-7} \frac{M_8}{\Gamma} \left(\frac{B}{G} \right)^2. \quad (24)$$

The differential equation (23) is solved by

$$\gamma_\pm^{-1}(\tilde{z}) = \gamma_{\pm i}^{-1} + K(\tilde{z} - \tilde{z}_i) \quad (24)$$

which is valid in the bounds

$$\begin{aligned} \gamma_{1\pm} &:= (\gamma_{1\pm i}^{-1} + K[\tilde{z} - \tilde{z}_i])^{-1} \leq \gamma_\pm \\ \gamma_\pm &\leq (\gamma_{2\pm i}^{-1} + K[\tilde{z} - \tilde{z}_i])^{-1} =: \gamma_{2\pm}. \end{aligned} \quad (25)$$

Considering conservation of particle number and inserting eq. (1) for the initial state leads to the resulting spectrum

$$n_\pm(\gamma_\pm, \tilde{z}) = N_\pm \gamma_\pm^{-2} (\gamma_\pm^{-1} - K[\tilde{z} - \tilde{z}_i])^{s-2} \quad (26)$$

From Fig. 7 we see that the particle spectrum influenced by synchrotron losses is well represented by a power law with the original spectral index between the cutoffs given by Eq. (25). But in contrast to the case of inverse Compton losses also the lower energy cutoff may be considerably lowered and the higher energy cutoff does not approach a fixed limit if the magnetic field strength remains constant along the jet, as we assumed.

A rough estimate for the blob's distance \tilde{z}_0 from the accretion disk plane at which the lower energy cutoff is significantly influenced by synchrotron losses may be achieved by setting $\gamma_{1\pm}(\tilde{z}_0) = \frac{\gamma_{1\pm i}}{2}$, yielding

$$\tilde{z}_0^{sy} := \tilde{z}_i + \frac{1}{\gamma_{1\pm i} K} \approx \tilde{z}_i + 2 \cdot 10^7 \frac{\Gamma_1}{\gamma_{1\pm i} M_8} \left(\frac{B}{G} \right)^{-2}. \quad (27)$$

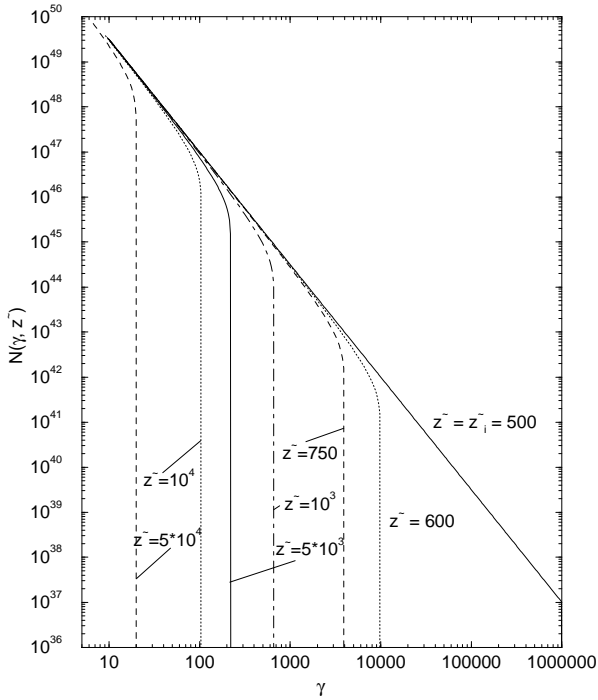


Fig. 7: Evolution of a power law particle energy spectrum affected by synchrotron losses. Parameters: $\tilde{z}_i = 500$, $\gamma_{1\pm i} = 10$, $\gamma_{2\pm i} = 10^6$, $s = 2.5$, $M_8 = 1$, $B = 3G$.

4.3. Bremsstrahlung losses

An estimation of particle energy losses due to relativistic e^+e^- and e^-e^- bremsstrahlung is obtained using the formalism similar to the one proposed by Dermer & Liang (1989) for power law particle spectra. In contrast to their calculation, we include the Doppler boosting of the bremsstrahlung photon assuming that it is emitted in the direction of one of the incoming particles. Furthermore, we use the ultrarelativistic limit of the bremsstrahlung cross section derived by Baier et al. (1967).

Results of this treatment are shown in Fig. 8 which shows that the single particle energy loss rate is roughly proportional to the particle energy so that the energy loss timescale remains roughly constant.

As we also see from our numerical calculations, there is no very significant dependence of the energy loss timescale on the lower cut-off of the particle distributions. Considering the lower energy end of the particle spectra, we find a typical energy loss timescale of the order

$$\tau_{br} = 5 \cdot 10^4 s \cdot n_{11}^{-1} \quad (28)$$

— where $n_{11} = \frac{n}{10^{11} \text{ cm}^{-3}}$ — which corresponds to a blob distance of

$$\tilde{z}_0^{br} = \tilde{z}_i + 10^3 \frac{\Gamma_1}{n_{11} M_8} \quad (29).$$

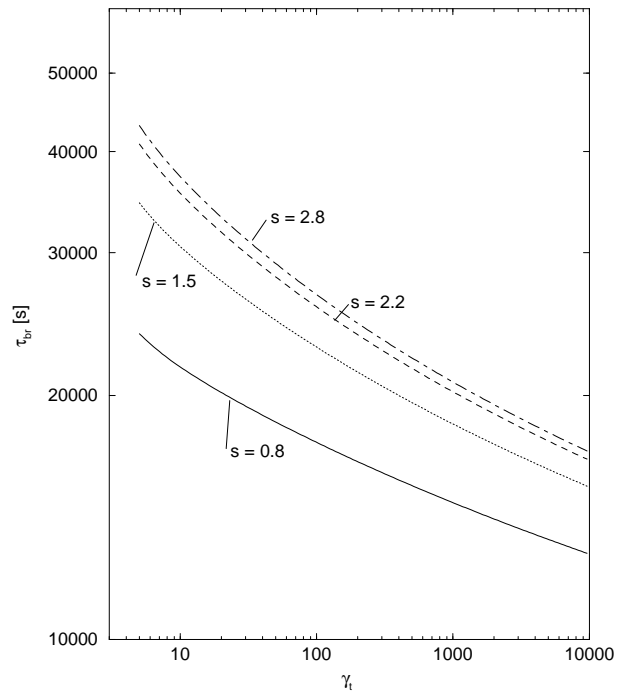


Fig. 8: Single particle energy loss timescales due to bremsstrahlung emission for different values of the particle spectral index; $n_{\pm} = 10^{11} \text{ cm}^{-3}$.

4.4. Thermalization

The thermalization timescale for a plasma described by a power law in particle energy is again estimated using the formalism of Dermer & Liang (1989) to calculate the single particle energy loss and gain, respectively, due to Møller and Bhabha scattering. The numerical results for Møller scattering for several values of the power law spectral index s are shown in Fig. 9; the difference between Møller and Bhabha scattering turns out to be negligible. We only consider the timescales under the initial conditions; synchrotron, inverse Compton and bremsstrahlung losses, of course, will alter the upper cut-off of the particle distributions and hence, they will lengthen the thermalization timescale for particles with lower energy.

Obviously, the lower energy end of the particle spectrum is most seriously affected by energy gain due to Møller scattering. From our numerical calculations we find the timescale for this energy exchange process as

$$\tau_{th} = 20 s \frac{\gamma_{1-} - \gamma_{1+}}{n_{11}} \quad (30)$$

corresponding to a distance

$$\tilde{z}_0^{th} = \tilde{z}_i + 0.4 \frac{\Gamma_1 \gamma_{1+} + \gamma_{1-}}{n_{11} M_8}. \quad (31)$$

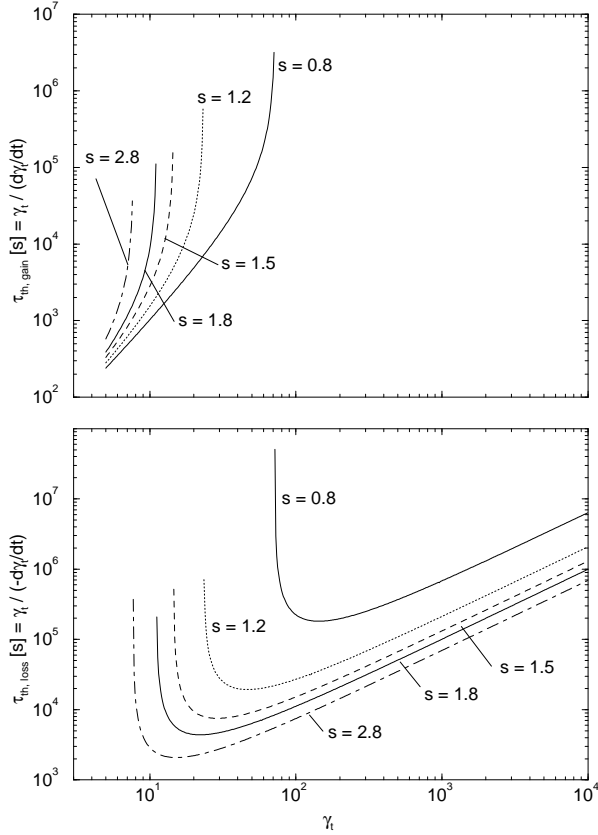


Fig 9: Timescales for single particle energy loss or gain, respectively due to Møller scattering; $n_{\pm} = 10^{11} \text{ cm}^{-3}$

4.5. Pair annihilation losses

In the general case, the particle loss rate can be written as

$$\left(\frac{dN^{\pm}(\gamma_{\pm}, \tilde{z})}{dt}\right)_{PA} = - \int_{V_B} dV n_{\pm}(\gamma_{\pm}, \tilde{z}) \cdot \int_{\gamma_{1\mp}}^{\gamma_{2\mp}} d\gamma_{\mp} n_{\mp}(\gamma_{\mp}, \tilde{z}) \bar{v}\bar{\sigma}(\gamma_{+}, \gamma_{-}) \quad (32)$$

which, in the ultrarelativistic limit and for a homogeneous blob, becomes

$$\left(\frac{dN^{\pm}(\gamma_{\pm}, \tilde{z})}{d\tilde{z}}\right)_{PA} = -N^{\pm}(\gamma_{\pm}, \tilde{z}) \frac{\lambda\pi r_e^2}{\Gamma\beta_{\Gamma}\gamma_{\pm}} \cdot \int_{\gamma_{1\mp}}^{\gamma_{2\mp}} d\gamma_{\mp} \frac{n_{\mp}(\gamma_{\mp}, \tilde{z})}{\gamma_{\mp}} (\ln[4\gamma_{+}\gamma_{-}] - 2). \quad (33)$$

where $N^{\pm}(\gamma_{\pm}, \tilde{z})$ is the spectral particle number and we used Svensson's formula (19 b) for the angle averaged reaction rate $\bar{v}\bar{\sigma}$.

In order to estimate the timescale for the evolution of initial power law particle spectra we may replace $n_{\mp}(\gamma_{\mp}, \tilde{z})$ by its initial value given by eq. (1). Then, the integral in eq. (33) is analytically solvable yielding

$$\left(\frac{dN^{\pm}(\gamma_{\pm}, \tilde{z})}{d\tilde{z}}\right)_{PA} = -N^{\pm}(\gamma_{\pm}, \tilde{z}) \frac{P n_{\mp}(\gamma_{\mp}, \tilde{z})}{\gamma_{1\mp}\gamma_{\pm}} \quad (34)$$

where, for spectral indices $2 \leq s \leq 3$, P may be roughly estimated by

$$P = \frac{(s-1)\lambda\pi r_e^2}{s\Gamma\beta_{\Gamma}} \left(\ln[4\gamma_{\pm}\gamma_{1\mp}] + \frac{1}{s} - 2 \right) \approx 10^{-12} \frac{M_8}{\Gamma} \text{ cm}^3 \quad (35)$$

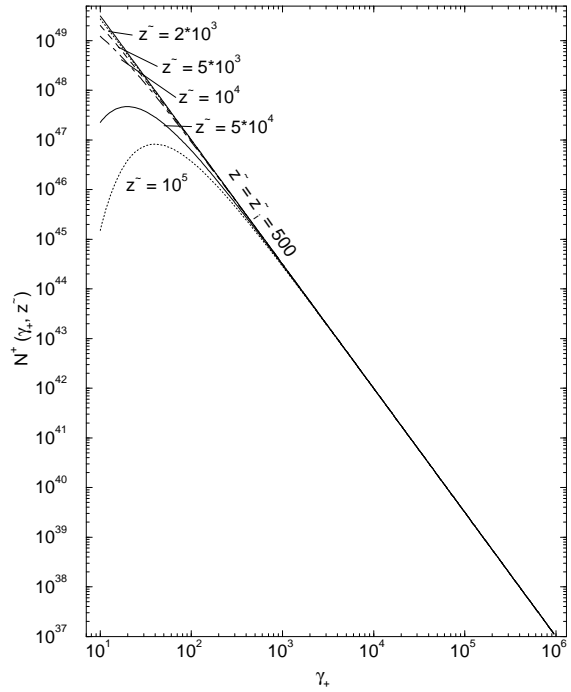


Fig. 10: Evolution of a power law particle energy spectrum influenced exclusively by pair annihilation losses in the case of an electron-dominated pair plasma. Parameters: $n_{-} = 10^{11} \text{ cm}^{-3} \gg n_{+}$, $\tilde{z}_i = 500$, $\gamma_{1\pm i} = 10$, $\gamma_{2\pm i} = 10^6$, $s = 2.5$, $M_8 = 1$, $\Gamma = 10$.

We now consider two special cases in which the differential equation (34) is easily solvable. First, we assume the pair plasma to be dominated by electrons (an $e^{-}p^{+}$ -plasma), thus $n_{-} \gg n_{+}$. Further neglecting geometrical effects on the extent of the plasma blob, we set $n_{-} = \text{const.}$, and obtain

$$N^{+}(\gamma_{+}, \tilde{z}) = N^{+}(\gamma_{+}, \tilde{z}_i) e^{-\frac{n_{-}P}{\gamma_{1-}\gamma_{+}}(\tilde{z}-\tilde{z}_i)} \quad (36)$$

which is shown in Fig. 10. From Eq. (36) we see the typical evolution time scale to be

$$\tilde{z}_0 = \tilde{z}_i + \frac{1}{A} \approx \tilde{z}_i + 10^{12} \frac{\Gamma \gamma_{1-} \gamma_{1+}}{M_8 n_- [cm^{-3}]}. \quad (37)$$

Secondly, we assume that electrons and positrons have the same particle density and distribution functions and again neglect geometrical effects eq. (34) becomes

$$\left(\frac{dN^\pm(\gamma_\pm, \tilde{z})}{d\tilde{z}} \right)_{PA} = -N^{\pm 2}(\gamma_\pm, \tilde{z}) \frac{P}{V_b \gamma_{1\mp} \gamma_\pm} \quad (38)$$

where V_b is the blob's volume. This is solved by

$$N^\pm(\gamma_\pm, \tilde{z}) = \frac{1}{c_0 + \frac{P \tilde{z}}{V_b \gamma_{1\mp} \gamma_\pm}}. \quad (39)$$

where the constant c_0 can be estimated by $\frac{1}{N^\pm(\gamma_\pm, \tilde{z}_i)}$. Thus we write

$$N^\pm(\gamma_\pm, \tilde{z}) = \frac{N^\pm(\gamma_\pm, \tilde{z}_i)}{1 + \frac{\tilde{z} - \tilde{z}_i}{\tilde{z}_0(\gamma_\pm)}}. \quad (40)$$

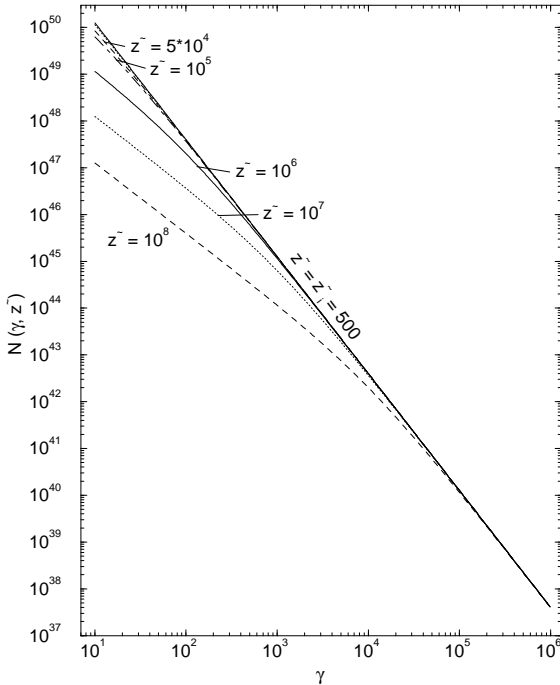


Fig. 11: Evolution of a power law particle energy spectrum influenced by pair annihilation losses in the case of electrons and positrons having the same density and distribution function. Parameters: $n_\pm = 10^{11} cm^{-3}$, $\tilde{z}_i = 500$, $\gamma_{1\pm i} = 10$, $\gamma_{2\pm i} = 10^6$, $s = 2.5$, $M_8 = 1$, $\Gamma = 10$.

This behavior which is, of course only self-consistent as long as the particle spectra may be well fitted by a power law with spectral index $\sim s$ is shown in Fig. 11. We derive the typical evolution timescale to be

$$\tilde{z}_0(\gamma_\pm) := \frac{\gamma_{1\pm}^3}{P n_\pm(\tilde{z}_i)} \approx 10^{12} \frac{\gamma_{1\pm}^3 \Gamma}{M_8 n_\pm(\tilde{z}_i) [cm^{-3}]}. \quad (41)$$

where we used $\frac{N^\pm(\gamma_\pm, \tilde{z}_i)}{V_b} = n_\pm(\gamma_\pm, \tilde{z}_i) \approx n_\pm \frac{(s-1) \gamma_{1\pm}^{s-1}}{\gamma_\pm^s}$.

4.6. Comparison of timescales

We now compare the typical timescales for particle spectra evolution by the energy loss and exchange processes considered above.

First, we see that the typical energy loss timescale for the inverse-Compton process is much shorter than for pair annihilation as well as for all the other processes considered above, but it only influences particles with energies above γ_∞ . Thus, it's negligible in calculations to the yield of pair annihilation radiation.

For the other processes, we estimated that

$$\tilde{z}_0 - \tilde{z}_i = \begin{cases} 10^2 \frac{\gamma_{1\pm}^3 \Gamma_1}{M_8 n_{11}} & \text{for PA, } n_+ = n_- \\ 10^2 \frac{\gamma_{1+} \gamma_{1-} \Gamma_1}{M_8 n_{11}^-} & \text{for PA, } n_+ \ll n_- \\ 10^7 \frac{\Gamma_1}{\gamma_{1\pm} M_8} \left(\frac{B}{G} \right)^{-2} & \text{for synchrotron} \\ 10^3 \frac{\Gamma_1}{n_{11} M_8} & \text{for bremsstrahlung} \\ 0.4 \frac{\Gamma_1 \gamma_{1+} \gamma_{1-}}{n_{11} M_8} & \text{for thermalization} \end{cases} \quad (42)$$

Comparing these timescales we see that for lower cutoffs $\lesssim 3$ the effect of bremsstrahlung losses are of minor importance to the particle spectra evolution. Particularly for the lower energy end of the particle spectrum, the bremsstrahlung losses are overestimated by the cross section approximation used in our calculation. So, this constraint will be eased when treating the bremsstrahlung emission process in more detail. But because of being much more efficient than bremsstrahlung emission energy gain due to Møller and Bhabha scattering will compensate the according energy losses.

As can be seen in Fig. 9, thermalization will affect the lower energy end of the particle spectra very seriously. But since it is no energy loss process and thus — by its nature — does not lead to a cooling of the plasma the latter will remain ultrarelativistic. This energy exchange process, of course, will alter the shape of the particle spectrum at low energies, but the mean energy of the particles remains constant, and the higher energy end of the particle spectrum will not suffer heavy energy losses. Thus, for a detailed discussion of the particle spectra evolution thermalization effects must be taken into account, but they do not seriously alter the shape of the time integrated annihilation spectrum.

Furthermore, we can derive a critical magnetic field strength for the dominance of synchrotron losses over pair annihilation losses on particle spectra evolution. This is given by

$$\left(\frac{B_{cr}}{G}\right)^2 = \begin{cases} 10^5 \frac{n_{\pm 1}}{\gamma_{i\pm}^2} & \text{for } n_+ = n_- \\ 10^5 \frac{n_{\pm 1}}{\gamma_{i+}^2 \gamma_{i-}} & \text{for } n_+ \ll n_- \end{cases} \quad (43)$$

If B is significantly lower than B_{cr} we may really neglect the effect of synchrotron cooling on the particle energy spectrum.

5. Comparison to the inverse-Compton spectrum

We now compare the yield of pair annihilation photons to the γ -ray spectrum produced by inverse-Compton scattering of accretion disk photons by the high energy particles of the jet. As we pointed out in section 4.6, this process is only efficient for high energy particles $\gamma > \gamma_\infty$, but works over a much shorter timescale than all the other processes occurring in the pair plasma. According to the long integration times of the observing instruments we only see time integrated spectra of AGN.

Thus, it is of interest to compare the time integrated inverse-Compton spectrum to the pair annihilation spectrum integrated over the typical timescale either for pair annihilation effects on the lower energy particles or for any other mechanism reducing the particle density of pairs near the lower energy cutoff.

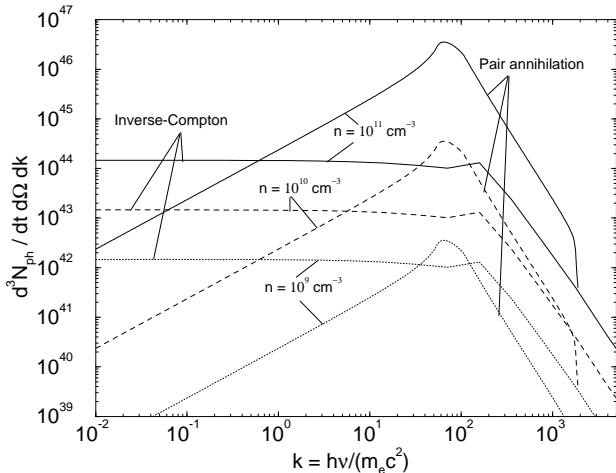


Fig. 12: Time-integrated inverse-Compton and pair annihilation spectra; parameters in the text.

For the following calculations, we assume this timescale to be of the order of $\tilde{z}_0 \sim 10^3$. Each plasma blob is assumed to be spherical with a radius of 10^{11} cm and injected at $\tilde{z}_i = 10$. The accretion disk radiates with $L_0 = 10^{46} \frac{erg}{s}$, and the mass of the central black hole is

$10^8 M_\odot$. The accretion disk radiation spectrum is modelled by a greybody distribution with a radial dependence of the temperature according to the accretion disk model of Payne and Eardley (1977). The lower energy cutoff of the distribution functions is $\gamma_{1\pm} = 3$, the higher cutoff is $\gamma_{2\pm} = 10^4$, and we assume that both electron and positron density are equal. The spectral index of the distribution functions is $s = 2$. The observing angle with respect to the jet axis is $\theta = 2^\circ$, and the blob moves outwards with a Lorentz factor of $\Gamma = 10$. These parameters are convenient to explain the γ -ray spectra of some γ -ray blazars by the inverse-Compton process.

The inverse-Compton radiation spectrum is calculated using the full Klein-Nishina cross section in the head-on approximation. The resulting photon number spectra from inverse-Compton scattering and pair annihilation are shown in Fig. 12 where we see that for particle densities $n \gtrsim 10^9 \text{ cm}^{-3}$ the contribution of pair annihilation should lead to an observable effect in the spectra. The flat inverse Compton spectrum at small photon energies is particularly noteworthy.

We attribute this mainly to the presence of a low-energy cutoff at $E_c = \gamma_c m c^2$ in the radiating particle distribution function. From the work of Schlickeiser (1982) it is well known that such a low-energy cutoff indeed leads to a flat scattered photon spectrum below the photon energy

$$E_\gamma^0 = \frac{4 \epsilon_0 \gamma_c^2}{1 + \frac{4 \epsilon_0 \gamma_c}{m c^2}} \approx 4 \epsilon_0 \gamma_c^2, \quad (44)$$

where ϵ_0 denotes the energy of the assumed monoenergetic target photon distribution function. (Corresponding calculations for extended target photon energy distributions by Schlickeiser [1980] showed similar flattenings.) According to Eqs. (14) and Fig. 1 of Schlickeiser (1982) the inverse Compton power of scattered photons varies proportional to

$$\chi(E_\gamma) \propto E_\gamma^{\frac{1-s}{2}} \quad \text{for } E_\gamma \geq E_\gamma^0 \quad (45a)$$

where s is the power-law index above E_c , while at energies $\epsilon_0 \leq E_\gamma \ll E_\gamma^0$ one obtains

$$\chi(E_\gamma) \propto \left(\frac{E_\gamma}{\epsilon_0}\right)^{\frac{1-s}{2}} \left(\frac{E_\gamma}{4 \epsilon_0 \gamma_c^2}\right)^{\frac{s+1}{2}} \propto \left(\frac{E_\gamma}{\epsilon_0}\right), \quad (45b)$$

indicating that indeed spectral breaks in the inverse Compton scattered photon spectrum by $\Delta\alpha = 1 - \frac{1-s}{2} = \frac{s+1}{2}$ around the intrinsic energy E_γ^0 are implied. Due to the blueshift by the relativistically moving blob this spectral break occurs at

$$k_c = \frac{4 \epsilon_0 \gamma_c^2}{m c^2} D(\mu^*) = 1.96 \left(\frac{\epsilon_0}{10 \text{ keV}}\right) \left(\frac{\gamma_c}{5}\right)^2 D(\mu^*) \quad (46)$$

with the Doppler factor

$$D(\mu^*) = \left[\Gamma(1 - \beta_\Gamma \mu^*)\right]^{-1}. \quad (47)$$

k_c lies in the MeV energy band which is in agreement with the inverse Compton curves in Fig. 12. With parameter values as chosen here, on top of this break the contribution from the pair annihilation radiation is located.

5.1. Comparison with observations

It can be seen from Fig. 12, that the pair annihilation emission in such a highly relativistic plasma does not result in a 511-keV peak. The annihilation radiation is blueshifted both, by the relativistic motion of the pairs in the blob rest frame, and by the Doppler boosting due to the bulk motion. The pair annihilation peaks near the photon energy

$$k_{max} = \gamma_1 D(\mu^*) \quad (48),$$

with the Doppler factor (47).

For the parameters chosen in Fig. 12 we obtain $k_{max} = 89.2$, so that the annihilation feature is at energies of $\sim 50 - 100 \text{ MeV}$. In this case the annihilation bump appears almost like the well-known (e. g. Cavallo & Gould 1971, Stecker 1973) γ -ray bump from decaying π^0 's near 70 MeV if they do not move relativistically. The detection of enhanced bumpy emission near 70 MeV from an AGN would therefore be no unique clue on the presence of hadrons in the source, but may point to blueshifted annihilation radiation.

However, for a sample of AGN sources seen under different viewing angles μ^* there will be quite some variation in the values of the parameters γ_1 , defining the low-energy cutoff of the relativistic electron and positron energy spectrum, and the relativistic bulk speed of the emitting blob, Γ , from source to source. While the energy exchange processes discussed in section 4, will keep the low-energy turnover of the distribution function at mildly relativistic values, $\gamma_1 \geq 3$, the wide dispersion in the Doppler factor (47) values will imply a corresponding wide distribution in the value of the annihilation peak energy (48). Although we have made no detailed effort so far to optimize parameters to explain individual source spectra, it is evident that in principle the inclusion of the annihilation radiation is capable to explain emission maxima and spectral breaks at MeV energies. The occurrence of spectral maxima between 1 and 10 MeV for the sources 3C273 and 3C279 has been reported by recent Comptel observations (Williams et al. 1995). An even more drastic example is the detection of the MeV-blazar GRO J0516-609 near PKS 0506-612/0522-611 by Bloemen et al. (1995). Our spectral modelling confirms the suggestion of Bloemen et al. that the MeV emission in this object represents the broad blue-shifted annihilation line.

A possible test for the hypothesis that the emission maxima in the observed γ -ray energy spectra are due to blueshifted annihilation radiation is offered by the predicted relation between the maximum photon energy (48) and the total γ -ray luminosity. Making the strong assumption, that apart from the Doppler factor all other intrinsic

physical parameters of the sources are equal, the total pair annihilation luminosity will scale with the Doppler factor as $L_p \propto D^3$. A similar Doppler factor dependence holds for the inverse-Compton luminosity (DS). Combined with Eq. (48) this implies the relation

$$k_{max} \propto L_p^{1/3} \quad (49),$$

i.e. the strong Doppler boosting in bright objects also blueshifts the annihilation peak to high photon energies.

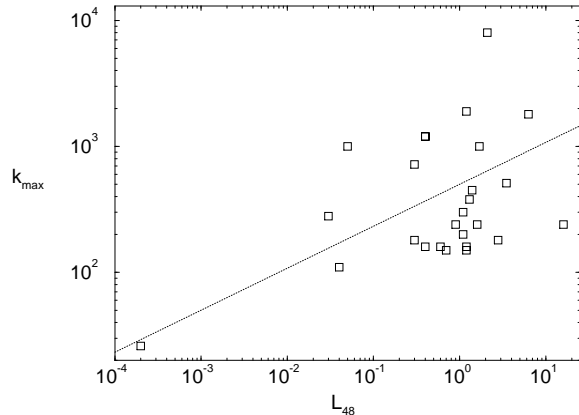


Fig. 13: Relation between MeV- γ -ray peak energy and total γ -ray luminosity for 33 AGN detected by EGRET.

We have used the available compilation of blazar energy spectra (Montigny et al. 1995) to estimate both the γ -ray luminosity L_p and the maximum photon energy (correcting for cosmological redshift), and the result is shown in Fig. 13 in comparison with the predicted correlation (49). The presently available data are not in contradiction with the hypothesis (49). A more stringent test would be possible if more AGNs with luminosities in the range $0.0005 - 0.03 L_{48}$ are detected with well-resolved γ -ray energy spectra.

6. Summary and conclusions

In this work we have calculated the contribution of the pair annihilation process in relativistic electron-positron jets to the γ -ray emission. Under the same assumptions as for the calculation of the yield of the inverse Compton scattered photons by relativistic particles in the jet (Dermer and Schlickeiser 1993) we calculated the emerging pair annihilation radiation taking into account all spectral broadening effects due to the energy spectra of the annihilating particles and the bulk motion of the jet. We started from the pair annihilation reaction rate in relativistic plasmas (Svenson 1982) and developed a new asym-

ptotic approximation appropriate for relativistic pair energies which provides a very accurate approximation of the pair annihilation spectrum for all photon energies.

The evolution of the particle energy spectra with time has been taken into account consistently, discussing in detail the role of inverse Compton losses, synchrotron losses, relativistic bremsstrahlung losses, pair annihilation losses and Møller and Bhabha thermalization. For typical blazar parameters two particle-number conserving loss processes dominate at large (Lorentz factor $\gamma > 10^3$) particle energies (inverse Compton losses) and at very low (Lorentz factor $\gamma < 30$) energies (thermalization), while the catastrophic pair annihilation losses reduce the number of radiating particles thus avoiding the "dead-electron-problem" (Begelman et al. 1984). We demonstrated that in spectral appearance the time-integrated pair annihilation spectrum appears almost like the well-known γ -ray spectrum from decaying π^0 -mesons at rest, since it yields a broad bumpy feature located between 50 and 100 MeV. Moreover, we demonstrated that for pair densities greater 10^{10} cm^{-3} in the jet the annihilation radiation will dominate the inverse Compton radiation, and due to its bump-like spectrum indeed may explain reported spectral bumps at MeV energies. The refined treatment of the inverse Compton radiation including Klein-Nishina cross section corrections, the low-energy cutoff in the radiating relativistic particle distribution function and a realistic greybody accretion disk target photon spectrum leads to spectral breaks of the inverse Compton emission in the MeV energy range with a change in spectral index $\Delta\alpha$ larger than 0.5 as detected in PKS 0528+134 and 3C273.

Acknowledgements We thank H. Mause for calculating the inverse Compton radiation spectra. Discussions with C. D. Dermer, F. Aharonian, M. Pohl and G. Henri are gratefully acknowledged. RS acknowledges partial support by the DARA (50 OR 94063) of his Compton observatory guest investigator programs. MB acknowledges financial support by the Deutsche Forschungsgemeinschaft.

References

- Baier, V. N., Fadin, V. S., Khoze, V. A., 1967, Soviet Physics JETP **24**, Nr. 4, 760
- Begelman, M. C., Blandford, R. D., Rees, M., 1984, Rev. Mod. Phys. **56**, 255
- Blandford, R. D., 1990, in: Active Galactic Nuclei (eds. T. Courvoisier, M. Mayor), Springer, New York, p. 161
- Blandford, R. D., 1993, in: Proc. of the Compton Symp. (eds. N. Gehrels, M. Friedlander, & J. P. Norris), AIP, New York, p. 533
- Blandford, R. D., Königl, A., 1979, ApJ **232**, 34
- Bloemen, H., Bennett, K., Blom, J. J., et al., 1995, AA **293**, L1
- Cavallo, G., Gould, R. J., 1971, Nuovo Cimento **2 B**, 77
- Coppi, P. S., Blandford, R. D., 1990, MNRAS **245**, 453
- Dermer, C. D., 1993, in: Proc. of the Compton Symp. (eds. N. Gehrels, M. Friedlander, & J. P. Norris), AIP, New York, p. 541
- Dermer, C. D., Gehrels, N. 1995, ApJ, in press
- Dermer, C. D., Liang, E. P., 1989, ApJ **339**, 512
- Dermer, C. D., Schlickeiser, R., 1992, Science **257**, 1642
- Dermer, C. D., Schlickeiser, R., 1993, ApJ **416**, 458 (DS)
- Dermer, C. D., Schlickeiser, R., 1994, ApJ Suppl. **90**, 945
- Henri, G., Pelletier, G., Roland, J., 1993, ApJ **404**, L41
- Kanbach, G., 1994, private communication
- Kurfess, J. D., 1994, in: Multi-wavelength continuum emission of AGN, eds. T.J.-L. Courvoisier, A. Blecha, Kluwer, Dordrecht, p. 39
- Lightman, A. P., Zdziarski, A. A., 1987, ApJ **319**, 643
- v. Mongitny, C., Bertsch, D. L., Chiang, J., et al., 1995, ApJ, in press
- Payne, D. G., Eardley, D. M., 1977, Ap Lett. **19**, 39
- Protheroe, R. J., Mastichiadis, A., Dermer, C. D. 1992, Astroparticle physics **1**, 113
- Scheuer, P.A.G., Readhead, A.C.S., 1979, Nature **277**, 182
- Schlickeiser, R., 1980, ApJ **240**, 636
- Schlickeiser, R., 1982, A & A **107**, 378
- Svensson, R., 1982, ApJ **258**, 321
- Stecker, F. W., 1973, ApJ **185**, 499
- Thompson, D., Bertsch, D. L., Dingus, B. L., et al., 1994, in: Multi-wavelength continuum emission of AGN, eds. T.J.-L. Courvoisier, A. Blecha, Kluwer, Dordrecht, p. 49
- Williams, O. R., Bennett, K., Bloemen, H., et al. 1995, AA , in press
- Zdziarski, A. A., Ghisellini, G., George, I. M., et al. 1990, ApJ **363**, L1